Editors' Suggestion

Dual Instability of Superconductivity from Oxygen Defects in $La_3Ni_2O_{7+\delta}$

Peiheng Jiang,[1,*] Jie Li,[2,*] Yu-Han Cao,[2,*] Xiaodong Cao,[3,4] Zhicheng Zhong,[3,4] Yi Lu,[2,5,†] and Qiang-Hua Wang[2,5,‡]
[1]School of Physics, MOE Key Laboratory for Nonequilibrium Synthesis and Modulation of Condensed Matter, Xi'an Jiaotong University, Xi'an 710049, China
[2]National Laboratory of Solid State Microstructures and School of Physics, Nanjing University, Nanjing 210093, China
[3]Suzhou Institute for Advanced Research, University of Science and Technology of China, Suzhou 215123, China
[4]School of Artificial Intelligence and Data Science, University of Science and Technology of China, Hefei 230026, China
[5]Collaborative Innovation Center of Advanced Microstructures, Nanjing University, Nanjing 210093, China

(Received 2 December 2025; accepted 24 August 2026; published 15 September 2026)

We uncover a dual mechanism by which oxygen defects suppress superconductivity in the bilayer nickelate $La_3Ni_2O_{7+\delta}$ using density functional theory, dynamical mean-field theory, and functional renormalization group analysis. Apical vacancies and interbilayer interstitials emerge as the dominant low-energy defect species and are further stabilized by orthorhombic domain walls. These two defect classes drive the electronic structure in opposing directions. Vacancy-induced disorder generates local magnetic moments and promotes Anderson localization at moderate concentrations, whereas periodic interstitial ordering yields a coherent but weakly correlated metallic background that fails to support superconductivity. These findings highlight the decisive role of oxygen defects in shaping superconductivity and provide microscopic guidance for improving it through controlled defect engineering.

DOI: 10.1103/vhgl-lpwv

Introduction—The discovery of superconductivity with $T_c \approx 80$ K in bulk $La_3Ni_2O_7$ under hydrostatic pressure [1–3] has sparked intense interest in nickelate superconductors (see Refs. [4,5] for recent reviews). From the outset, oxygen stoichiometry emerged as a central factor, with early studies identifying oxygen vacancies [6] as a likely source of the low superconducting volume fractions in initial samples [7]. Despite steady improvements in synthesis, reliably stabilizing the pressurized superconducting phase remains challenging [8–12]. At ambient pressure, superconductivity has thus far been realized only in epitaxially strained thin films [13,14].

A natural approach to improving sample quality is to remove oxygen vacancies through postgrowth annealing [15,16]. This procedure, however, has revealed a deeper puzzle. High-pressure oxygen annealing drives the material toward stoichiometric $La_3Ni_2O_7$ and improves ambient-pressure metallicity, yet it can simultaneously suppress superconductivity even under pressure [11,17]. This paradox indicates that restoring the average oxygen content is insufficient and that annealing can stabilize competing structural or electronic states that are unfavorable for pairing. Supporting this view, near-field microscopy reports stripelike structural variations linked to local oxygen inhomogeneity [18], and atomic-resolution imaging identifies interstitial oxygen in nonsuperconducting samples, implicating excess or redistributed oxygen as a key control parameter [19]. These observations point to oxygen as an active degree of freedom even in annealed samples, yet the microscopic connection between specific defect configurations and suppressed superconductivity remains unresolved.

Unraveling this connection requires determining how oxygen defects are stabilized and how they reshape the correlated electronic landscape. In this Letter, we address this by combining density functional theory (DFT) to resolve defect energetics, dynamical mean-field theory (DMFT) to capture their impact on local correlations and coherence, and functional renormalization group (FRG) to assess the resulting superconducting tendencies. DFT identifies apical vacancies and interstitials as universal low-energy defects, whose asymmetric strain fields tend to separate them in space. Both species are further stabilized by orthorhombic domain walls at ambient pressure. DMFT shows that vacancies degrade electronic coherence and promote local Mott states and magnetic moments; the resulting site dilution drives Anderson localization. Conversely, interstitials arrange periodically to produce a coherent but weakly correlated metallic background. FRG reveals that this oxygen-rich metal fails to develop the robust $s_{\pm}$-wave pairing seen in stoichiometric $La_3Ni_2O_7$. These results establish a dual mechanism for the suppression of superconductivity in vacancy-rich or interstitial-rich regions, one that plausibly extends to nominally stoichiometric samples through their oxygen inhomogeneity, and indicate that the intrinsic high-T_c phase is best realized by

*These authors contributed equally to this work.
†Contact author: yilu@nju.edu.cn
‡Contact author: qhwang@nju.edu.cn

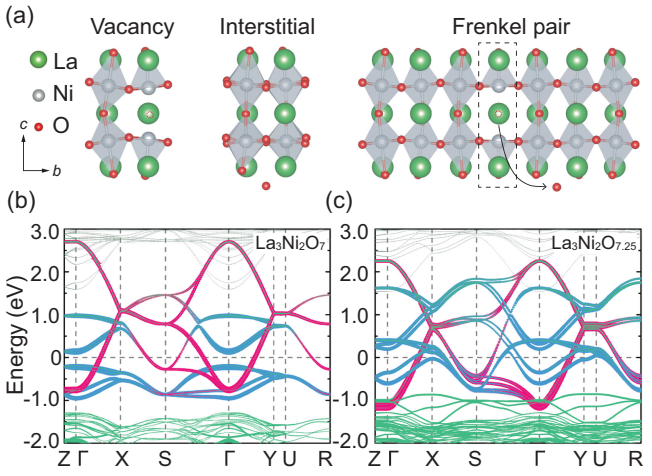

FIG. 1. (a) Schematic structures of oxygen defects in $La_3Ni_2O_7$. The dashed box marks the boundary between two orthorhombic domains. (b),(c) DFT + U band structures of (b) pristine $La_3Ni_2O_7$ and (c) $La_3Ni_2O_{7.25}$. Magenta, cyan, and green indicate Ni $d_{x^2-y^2}$, $d_{3z^2-r^2}$, and O p orbital character, respectively.

suppressing vacancy disorder while strictly preventing interstitial accumulation.

Oxygen vacancies and interstitials—To determine the energetics of oxygen defects, we performed DFT$(+U)$ calculations using the Vienna *ab initio* simulation package (VASP) [20,21] with the Perdew-Burke-Ernzerhof functional [22]. An effective $U = 4.0$ eV was adopted, consistent with previous studies that reproduce the experimental crystal structure and Fermi surface [1,23]. Figure 1(a) illustrates the defect types considered, namely vacancies, interstitials, and their combination into charge-neutral Frenkel pairs. Multiple candidate locations were examined for each defect type. Energetics identify the inner apical site as the most favorable position for a vacancy [24], while interstitial oxygen preferentially resides between two nickel-oxygen bilayers. These configurations match the dominant defect species observed experimentally [6,19]. Further computational details are provided in Supplemental Material (SM) [25].

The calculated formation energies show that $La_3Ni_2O_7$ readily accommodates both oxygen deficiency and excess. Vacancy formation is moderately costly (2.35 eV), comparable to high-valence transition-metal (e.g., Ni^{3+} or Fe^{4+}) oxides that are prone to oxygen loss [30], implying that vacancies can persist in as-grown samples. By contrast, interstitial oxygen exhibits a large negative formation energy (−1.22 eV), indicating a strong thermodynamic tendency toward oxygen uptake. While the formation energy of a Frenkel pair confined to a single unit cell is relatively high at 1.42 eV, placing the vacancy and interstitial a few unit cells apart lowers it by 0.53 to 0.89 eV, significantly lower than in benchmark oxide ion conductors [31], pointing to a labile oxygen sublattice susceptible to intrinsic disorder. Notably, the structural impact of these defects is markedly asymmetric. A vacancy contracts the c axis by only 0.5%, whereas an interstitial induces a substantial 3.5% reduction [25]. Consequently, the vacancies, with weak strain fields and weak mutual interactions [25], are expected to remain dispersed and disordered, consistent with microscopy [6], whereas the large strain around the interstitials favors their clustering into ordered, interstitial-rich regions, supported by our slab calculations [25] and recent microscopy [19].

These defect energetics are further reshaped by extended structural motifs, most notably domain walls. At ambient pressure, orthorhombic $La_3Ni_2O_7$ hosts low-energy domain walls formed by reversals of the octahedral rotation pattern along the b axis [Fig. 1(a)], stabilized at only 3.5 meV/Å^2 [25]. Our calculations identify these boundaries as effective defect traps. The formation energy of a vacancy drops by 0.37 eV when located on the wall, whereas that of an interstitial decreases by 0.23 eV when placed in the bulklike regions between the walls. This cumulative stabilization reduces the Frenkel pair energy near a wall to just 0.31 eV. These lowered energies indicate that the wall geometry stabilizes both defect species at their different preferred positions. The result is a possible multiscale inhomogeneity, with local vacancy disorder and interstitial ordering superimposed on larger-scale oxygen variations modulated by the walls. This provides a plausible microscopic origin for the stripelike conductivity modulations observed in $La_3Ni_2O_{7+\delta}$ [18].

Single-particle electronic structure with defects—Motivated by the energetic penalty for confined Frenkel pairs and the strain-driven clustering of interstitials, we model spatially separated oxygen-rich and oxygen-deficient environments through separate limiting structures and examine how each reshapes the local electronic structure. Figures 1(b) and 1(c) compare the DFT + U band structure of pristine $La_3Ni_2O_7$ with that of an interstitial-rich configuration $La_3Ni_2O_{7.25}$ in which one interbilayer region is fully occupied by interstitial oxygen. Interstitials shorten the surrounding apical Ni-O bonds and strongly increase interorbital hybridization, pushing the $d_{3z^2-r^2}$ (hereafter d_z) bands upward relative to $d_{x^2-y^2}$ (d_x) and enhancing their dispersion. Conversely, removing an inner-apical oxygen converts adjacent NiO_6 octahedra into NiO_5 square pyramids [Fig. 1(a)], lowers the local d_z level and suppresses intrabilayer hybridization. The characteristic d_z bonding-antibonding splitting then collapses, and the associated d_z states sink to the bottom of the e_g manifold, well below the Fermi level [25].

To quantify these changes, we constructed maximally localized Wannier functions [32,33] for d_x and d_z and extracted crystal-field splittings and orbital occupations for the limiting oxygen-deficient ($La_3Ni_2O_{6.5}$) and oxygen-rich ($La_3Ni_2O_{7.5}$) structures (Table I), which also serve as inputs for the correlated calculations below. In pristine $La_3Ni_2O_7$,

TABLE I. Crystal-field splittings and orbital-resolved occupations for $La_3Ni_2O_{7+\delta}$ ($\delta = 0, \pm 0.5$) at 0 (top) and 20 GPa (bottom). DMFT results were obtained at $T = 116$ K. Ill-defined entries are shown as ⋯.

		DFT			DMFT			
δ	Site	Δ	n_x	n_z	n_x	n_z	Z_x	Z_z
0 GPa								
0		0.25	0.67	0.83	0.67	0.83	0.42	0.27
−0.5	Pyramidal	1.55	0.49	1.98	0.96	1.03	⋯	⋯
−0.5	Octahedral	0.01	0.63	0.90	1.01	1.00	⋯	⋯
0.5		−0.09	0.63	0.37	0.61	0.39	0.54	0.66
20 GPa								
0		0.33	0.63	0.87	0.66	0.84	0.55	0.36
−0.5	Pyramidal	1.79	0.52	1.97	0.49	1.58	0.29	0.39
−0.5	Octahedral	0.04	0.60	0.91	0.96	0.97	0.15	0.19
0.5		−0.10	0.63	0.37	0.61	0.39	0.60	0.70

the splitting $\Delta = \epsilon_x - \epsilon_z$ is modest, producing a moderate polarization toward d_z with $n_z = 0.83$ close to half filling. In the vacancy-rich $La_3Ni_2O_{6.5}$, the pyramidal sites develop a large positive splitting ($\Delta = 1.55$ eV) that nearly saturates the d_z orbital ($n_z = 1.98$), whereas the octahedral sites remain similar to the stoichiometric limit with a weaker anisotropy. The imbalance in local hybridizations results in a pronounced charge disproportionation, with about 2.5 e_g electrons on the pyramidal sites and 1.5 on the octahedral sites. Oxygen-rich $La_3Ni_2O_{7.5}$, on the other hand, inverts the ordering of the e_g levels ($\Delta = -0.09$ eV), driving n_z down to 0.37 as the total e_g filling drops to 1.0 per Ni. These crystal-field shifts, hybridization changes, and charge redistributions persist under high pressure without altering the qualitative hierarchy for all three compositions.

Correlated electronic structure—Building on the DFT analysis, we now examine how oxygen defects reshape the correlated electronic states of $La_3Ni_2O_{7+\delta}$, laying the foundation for understanding their effects on superconductivity. DMFT calculations were performed using the TRIQS library [25,34–37] with a rotationally invariant Kanamori interaction ($U = 3.4$ eV, $J_H = 0.6$ eV [38]) at $T = 116$ K (inverse temperature $\beta = 100$). For pristine $La_3Ni_2O_7$ [Fig. 2(a)], the spectral functions remain qualitatively robust against pressure, showing typical characteristics of a Hund's metal [39], with narrow quasiparticle peaks at the Fermi level and broad Hubbard bands at higher energies [38,40–44]. The imaginary parts of the self-energies [Fig. 2(e)] are reduced under high pressure, indicating bandwidth-driven weakening of correlations. They remain larger for d_z than for d_x, showing pronounced orbital differentiation. The quasiparticle weights $Z = [1 - \partial \mathrm{Re}\Sigma(i\omega)/\partial\omega|_{\omega\to 0}]^{-1}$ are extracted as $Z_x = 0.42$ and $Z_z = 0.27$ at ambient pressure. These correspond to mass enhancements of about 2 and 4, respectively, in good agreement with angle-resolved photoemission spectroscopy measurements [23].

For the vacancy-rich $La_3Ni_2O_{6.5}$, correlations drastically reshape the electronic landscape. As shown in Table I, local Coulomb interactions largely suppress the DFT-predicted charge disproportionation, restoring a filling of $n \approx 2$ on both site types and eliminating the strong orbital polarization at the pyramids, bringing the local e_g orbitals close to half filling, where correlations generally favor Mott-insulating behavior. Accordingly, at ambient pressure, the d_x orbital on the pyramidal sites is pushed to the verge of a Mott transition, consistent with its nearly divergent self-energy [Fig. 2(f)]. Although the narrower d_z band might be expected to be even more prone to a Mott transition, its

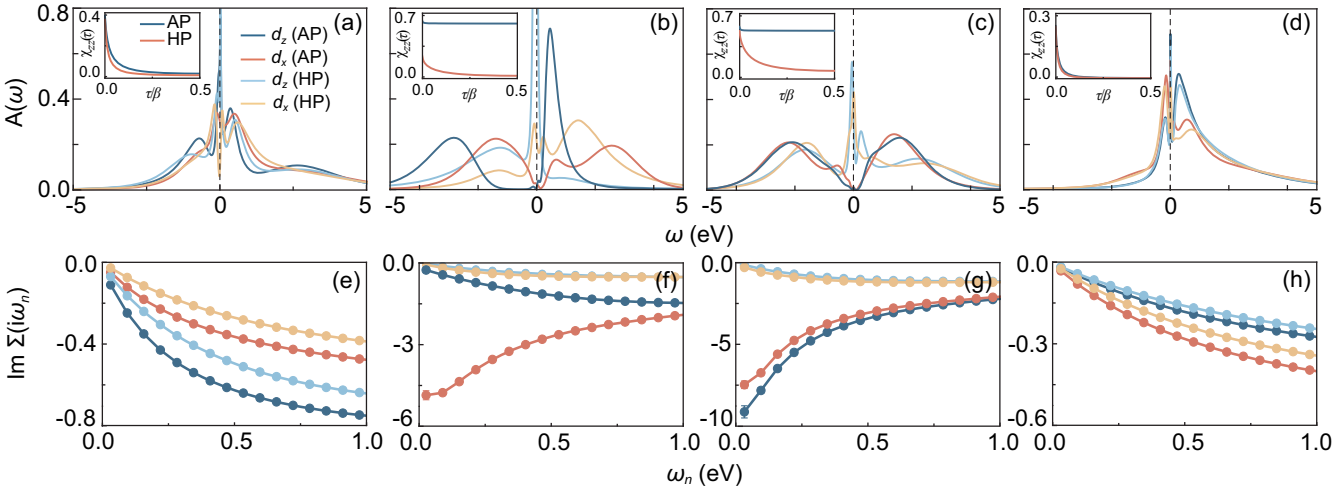

FIG. 2. DMFT spectral functions (a)–(d) and self-energies (e)–(h) for $La_3Ni_2O_7$ [(a),(e)], $La_3Ni_2O_{6.5}$ [(b),(f) pyramidal sites; (c),(g) octahedral sites], and $La_3Ni_2O_{7.5}$ [(d),(h)] under ambient pressure (AP, 0 GPa) and high pressure (HP, 20 GPa). Insets in panels (a)–(d) show the imaginary-time spin-spin correlation functions $\chi_{zz}(\tau) = \langle S_z(\tau)S_z(0)\rangle$, where S_z is the total z spin component of the d_x and d_z orbitals.

deeper onsite energy leaves it slightly electron doped and places the chemical potential on the inner edge of its upper Hubbard band [45,46]. The d_z orbital therefore retains only a small, incoherent spectral weight at the Fermi level [Fig. 2(b)], with $-\mathrm{Im}\,\Sigma(i\omega \to 0) \approx 0.13$ eV far exceeding the thermal scale $k_B T \approx 10$ meV, signaling non-Fermi-liquid behavior rather than a coherent metal. In contrast, the octahedral sites become fully Mott insulating, displaying gapped spectra and divergent self-energies [Figs. 2(c) and 2(g)]. The spin correlation function $\chi_{zz}(\tau) \equiv \langle S_z(\tau) S_z(0) \rangle$ reveals robust frozen moments on both sublattices. The equal-time value $\chi_{zz}(0) \approx 2/3$ corresponds to an instantaneous effective moment $S_{\mathrm{eff}} \approx 1$, while the negligible decay at $\tau = \beta/2$ signifies that these moments are essentially unscreened [47]. The formation of these robust local moments is a direct consequence of the disrupted intrabilayer hybridization at the pyramidal sites combined with the effective doping toward half filling. Under high pressure, a uniform vacancy lattice maintains sufficient coherence to screen these moments and recover a metallic state [Figs. 2(b) and 2(c), 2(f), and 2(g)]. However, as our DFT analysis implies, the vacancies remain disordered at the local scale in realistic samples. As detailed in SM [25], modeling the resulting site dilution and potential disorder reveals an Anderson localized state at moderate concentrations. This mechanism naturally accounts for the experimentally observed magnetic insulating behavior in oxygen-deficient samples, even under pressure [48], and aligns with the Anderson-localization characteristics found in transport measurements [49]. Sufficiently vacancy-rich regions thus cease to host the coherent carriers that pairing requires, precluding superconductivity.

In oxygen-rich $La_3Ni_2O_{7.5}$, representing the ordered interstitial-rich regions, the reduced e_g filling weakens electronic correlations relative to $La_3Ni_2O_7$. The Hubbard bands are strongly suppressed in the spectral function [Fig. 2(d)], and the imaginary parts of the self-energies are much smaller [Fig. 2(h)]. Orbital differentiation is effectively eliminated, yielding large and nearly equal quasiparticle weights (Table I). The increased quasiparticle weights, together with the reduced scattering rates $\tau^{-1} \approx -2Z\,\mathrm{Im}\,\Sigma(0^+)$, signal a highly coherent metal. This coherence is further reflected in the fully screened local spin response. The static impurity susceptibility $\chi_{\mathrm{imp}} = \int_0^\beta d\tau \chi_{zz}(\tau)$ drops to 1.3 and 1.0 eV^{-1} at 0 and 20 GPa, respectively, much smaller than in pristine $La_3Ni_2O_7$ under the same conditions (5.2 and 3.0 eV^{-1}). These results suggest that oxygen intercalation shifts the system toward the weak-coupling limit, placing $La_3Ni_2O_{7.5}$ in a parameter regime where low-energy instabilities arise, if at all, from residual Fermi-surface interactions rather than from strong local correlations.

Oxygen-tuned superconductivity—Motivated by the weak correlation revealed by DMFT for $La_3Ni_2O_{7.5}$, we employ singular-mode FRG (SM-FRG) [50–52] to analyze its low-energy instabilities and superconducting tendencies relative to pristine $La_3Ni_2O_7$ under high pressure. In SM-FRG, the one-particle-irreducible four-point vertex Γ_Λ is projected onto scattering matrices between fermion bilinears in the superconducting (SC), spin-density-wave (SDW), and charge-density-wave (CDW) channels, whose flow is then tracked as a function of a running infrared cutoff Λ. An instability is signaled when the most negative singular value S_Λ in one channel diverges at a critical scale Λ_c, which serves as an estimate of the associated transition temperature. This approach provides an unbiased treatment of competing ordering channels in the weak-to-moderate interaction regime [53–56] and has previously captured the $s_\pm$ superconducting state in bilayer and trilayer nickelates and its pressure evolution [57–60]. Additional details are provided in SM [25].

The calculations use the same Kanamori interaction form as in DMFT, with U and J_H varied to map the leading electronic instabilities. The resulting phase diagram for $La_3Ni_2O_{7.5}$ is shown in Fig. 3(a), with that of stoichiometric $La_3Ni_2O_7$ presented for comparison in Fig. 3(b). For $La_3Ni_2O_{7.5}$, no divergence is found in any channel down to the lowest cutoff $\Lambda = 10^{-4}$ eV, implying that any instability, if present, would occur only below $T_c \sim 1$ K. A noticeable SDW tendency appears only at larger J_H. Pristine $La_3Ni_2O_7$, by contrast, hosts a robust $s_\pm$-wave superconducting phase at small and moderate J_H, and similarly develops an SDW instability at larger J_H, but at

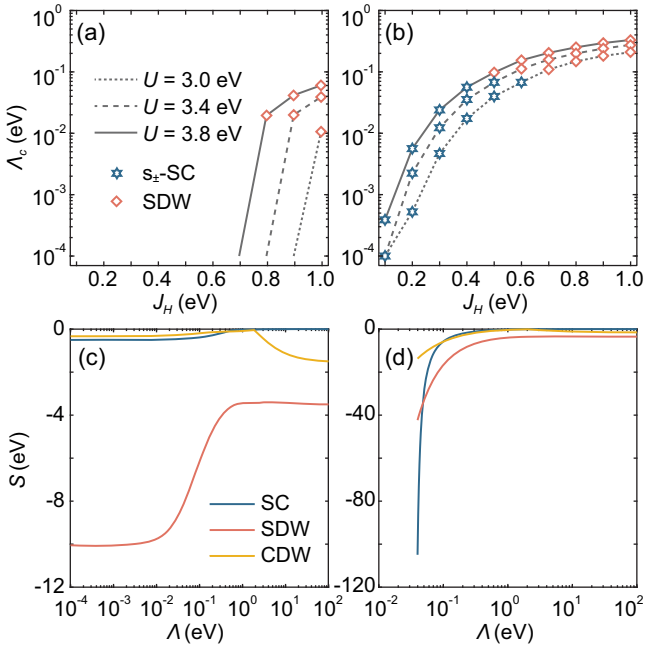

FIG. 3. Critical scales Λ_c as a function of J_H for different U values in (a) $La_3Ni_2O_{7.5}$ and (b) $La_3Ni_2O_7$. Panels (c) and (d) show representative flows of the singular values S in the SC, SDW, and CDW channels for $(U, J_H) = (3.0, 0.5)$ eV in $La_3Ni_2O_{7.5}$ and $La_3Ni_2O_7$, respectively.

substantially higher energy scales. This comparison makes clear that oxygen-rich $La_3Ni_2O_{7.5}$ shows a pronounced suppression of both magnetic and superconducting tendencies relative to pristine $La_3Ni_2O_7$.

To further clarify the origin of the contrasting phase diagrams, we show representative SM-FRG flows for $La_3Ni_2O_{7.5}$ and $La_3Ni_2O_7$ in Figs. 3(c) and 3(d), using $U = 3.0$ eV and $J_H = 0.5$ eV. Both systems behave similarly at large cutoff Λ. The bare Coulomb repulsion suppresses the CDW channel, seen in the decreasing S_{CDW}, and it prevents the development of an attractive SC channel, leaving the SDW channel dominating the initial flow. Around $\Lambda \sim 1$ eV, spin fluctuations strengthen the SDW channel and, through interchannel coupling, also enhance the CDW and SC channels. The crucial difference emerges at lower energy. In $La_3Ni_2O_{7.5}$, all three channels eventually saturate and no divergence appears down to 10^{-4} eV, which leads to the absence of an instability in Fig. 3(a). In $La_3Ni_2O_7$, however, the SDW fluctuations remain much stronger and significantly reinforce the SC channel through the Kohn-Luttinger mechanism [61], ultimately driving a Cooper instability. Together, these flow behaviors show that excess oxygen suppresses the superconducting instability in $La_3Ni_2O_{7.5}$ by weakening the SDW channel and the associated spin fluctuations that mediate pairing. Notably, the residual SDW tendency in $La_3Ni_2O_{7.5}$ favors interlayer *ferromagnetic* correlations, in stark contrast to the interlayer antiferromagnetic pattern of pristine $La_3Ni_2O_7$, providing a clear magnetic signature of oxygen-rich regions. Together with the vacancy-driven localization above, this reveals a dual mechanism by which oxygen defects suppress superconductivity.

Summary and discussion—Our analysis establishes that high-T_c superconductivity in $La_3Ni_2O_{7+\delta}$ is confined to a narrow stability window bounded by two defect-driven regimes. On one side, thermodynamically accessible oxygen vacancies degrade coherence and introduce disorder, which drives Anderson localization at moderate concentrations. On the other, the accumulation of interstitials stabilizes a coherent but weakly correlated Fermi liquid where the correlations essential for pairing are diluted. This microscopic dichotomy resolves the paradox of oxygen-annealed samples, where aggressive annealing successfully removes fatal vacancies but can inadvertently populate interstitial sites, driving the system into a nonsuperconducting metallic state. Moreover, given the strong local variations of oxygen content observed in real crystals [6], annealed samples may simultaneously host vacancy-rich and interstitial-rich regions, where the two branches of the dual mechanism operate in parallel, obstructing the formation of a coherent superconducting state even when the average composition is close to $\delta = 0$.

Practical optimization therefore demands breaking this trade-off. Beyond precise control of oxygen partial pressure during synthesis, our structural analysis suggests two specific routes for defect engineering. First, since interstitials induce a substantial c-axis contraction, applying strain to oppose this distortion could destabilize interstitial formation without hindering vacancy removal. Second, given that domain walls significantly lower defect formation energies, detwinning protocols [62] could eliminate these energetic traps, thereby widening the window for stoichiometric superconductivity.

Acknowledgments—We thank Jian-Xin Li, Meng Wang, Motoharu Kitatani, and Qing Li for insightful discussions. This work was supported by the National Key R&D Program of China (No. 2022YFA1403000 and No. 2024YFA1408100), the National Natural Science Foundation of China (No. 12274207, No. 12374147, No. 12574069, and No. 92365203), and the Basic Research Program of Jiangsu Province (No. BK20253009, No. BK20253012, and No. BK20233001). P. J. also acknowledges support from the Natural Science Basic Research Program of Shaanxi Province (No. 2025JC-YBQN-001), the Young Talent Support Project of Xi'an Jiaotong University (No. WL6J022), and the HPC Platform at Xi'an Jiaotong University.

Data availability—All data that support the findings of this study are available from the corresponding authors upon reasonable request.

[1] H. Sun, M. Huo, X. Hu, J. Li, Z. Liu, Y. Han, L. Tang, Z. Mao, P. Yang, B. Wang, J. Cheng, D.-X. Yao, G.-M. Zhang, and M. Wang, Signatures of superconductivity near 80 K in a nickelate under high pressure, Nature (London) **621**, 493 (2023).

[2] J. Hou, P.-T. Yang, Z.-Y. Liu, J.-Y. Li, P.-F. Shan, L. Ma, G. Wang, N.-N. Wang, H.-Z. Guo, J.-P. Sun, Y. Uwatoko, M. Wang, G.-M. Zhang, B.-S. Wang, and J.-G. Cheng, Emergence of high-temperature superconducting phase in pressurized $La_3Ni_2O_7$ crystals, Chin. Phys. Lett. **40**, 117302 (2023).

[3] Y. Zhang, D. Su, Y. Huang, Z. Shan, H. Sun, M. Huo, K. Ye, J. Zhang, Z. Yang, Y. Xu, Y. Su, R. Li, M. Smidman, M. Wang, L. Jiao, and H. Yuan, High-temperature superconductivity with zero resistance and strange-metal behaviour in $La_3Ni_2O_{7-\delta}$, Nat. Phys. **20**, 1269 (2024).

[4] M. Wang, H.-H. Wen, T. Wu, D.-X. Yao, and T. Xiang, Normal and superconducting properties of $La_3Ni_2O_7$, Chin. Phys. Lett. **41**, 077402 (2024).

[5] Y. Wang, K. Jiang, J. Ying, T. Wu, J. Cheng, J. Hu, and X. Chen, Recent progress in nickelate superconductors, Natl. Sci. Rev. **12**, nwaf373 (2025).

[6] Z. Dong, M. Huo, J. Li, J. Li, P. Li, H. Sun, L. Gu, Y. Lu, M. Wang, Y. Wang, and Z. Chen, Visualization of oxygen vacancies and self-doped ligand holes in $La_3Ni_2O_{7-\delta}$, Nature (London) **630**, 847 (2024).

[7] Y. Zhou, J. Guo, S. Cai, H. Sun, C. Li, J. Zhao, P. Wang, J. Han, X. Chen, Y. Chen, Q. Wu, Y. Ding, T. Xiang, H.-k.

Mao, and L. Sun, Investigations of key issues on the reproducibility of high-T_c superconductivity emerging from compressed $La_3Ni_2O_7$, Matter Radiat. Extremes **10**, 027801 (2025).

[8] N. Wang *et al.*, Bulk high-temperature superconductivity in pressurized tetragonal $La_3Ni_2O_7$, Nature (London) **634**, 579 (2024).

[9] G. Wang, N. N. Wang, X. L. Shen, J. Hou, L. Ma, L. F. Shi, Z. A. Ren, Y. D. Gu, H. M. Ma, P. T. Yang, Z. Y. Liu, H. Z. Guo, J. P. Sun, G. M. Zhang, S. Calder, J.-Q. Yan, B. S. Wang, Y. Uwatoko, and J.-G. Cheng, Pressure-induced superconductivity in polycrystalline $La_3Ni_2O_{7-\delta}$, Phys. Rev. X **14**, 011040 (2024).

[10] J. Li, D. Peng, P. Ma, H. Zhang, Z. Xing, X. Huang, C. Huang, M. Huo, D. Hu, Z. Dong, X. Chen, T. Xie, H. Dong, H. Sun, Q. Zeng, H.-k. Mao, and M. Wang, Identification of superconductivity in bilayer nickelate $La_3Ni_2O_7$ under high pressure up to 100 GPa, Natl. Sci. Rev. **12**, nwaf220 (2025).

[11] M. Shi, D. Peng, Y. Li, S. Yang, Z. Xing, Y. Wang, K. Fan, H. Li, R. Wu, B. Ge, Z. Zeng, Q. Zeng, J. Ying, T. Wu, and X. Chen, Spin density wave rather than tetragonal structure is prerequisite for superconductivity in $La_3Ni_2O_{7-\delta}$, Nat. Commun. **16**, 9141 (2025).

[12] F. Li *et al.*, Bulk superconductivity up to 96 K in pressurized nickelate single crystals, Nature (London) **649**, 871 (2026).

[13] E. K. Ko, Y. Yu, Y. Liu, L. Bhatt, J. Li, V. Thampy, C.-T. Kuo, B. Y. Wang, Y. Lee, K. Lee, J.-S. Lee, B. H. Goodge, D. A. Muller, and H. Y. Hwang, Signatures of ambient pressure superconductivity in thin film $La_3Ni_2O_7$, Nature (London) **638**, 935 (2025).

[14] G. Zhou, W. Lv, H. Wang, Z. Nie, Y. Chen, Y. Li, H. Huang, W.-Q. Chen, Y.-J. Sun, Q.-K. Xue, and Z. Chen, Ambient-pressure superconductivity onset above 40 K in $(La, Pr)_3Ni_2O_7$ films, Nature (London) **640**, 641 (2025).

[15] Y. Liu, E. K. Ko, Y. Tarn, L. Bhatt, J. Li, V. Thampy, B. H. Goodge, D. A. Muller, S. Raghu, Y. Yu, and H. Y. Hwang, Superconductivity and normal-state transport in compressively strained $La_2PrNi_2O_7$ thin films, Nat. Mater. **24**, 1221 (2025).

[16] Y. Zhang, C. Pei, N. Guo, L. Fan, M. Zhang, L. Wang, G. Zhang, F. Li, Y. Wang, C. Ma, W. Cheng, S. Wang, Q. Zheng, Y. Qi, and J. Zhang, Strong oxidizing annealing of bilayer $La_3Ni_2O_{7-\delta}$ results in suppression of superconductivity under high pressure, J. Solid State Chem. **355**, 125757 (2026).

[17] M. Huo, P. Ma, C. Huang, X. Huang, H. Sun, and M. Wang, Low volume fraction of high-T_c superconductivity in $La_3Ni_2O_7$ at 80 K and ambient pressure, arXiv:2501.15929.

[18] X. Zhou, W. He, K. Ni, M. Huo, D. Hu, Y. Zhu, E. Zhang, Z. Jiang, S. Zhang, S. Su, J. Jiang, Y. Yan, Y. Wang, D. Shen, X. Liu, J. Zhao, M. Wang, Z. Du, and D. Feng, Revealing nanoscale structural phase separation in $La_3Ni_2O_{7-\delta}$ single crystal via scanning near-field optical microscopy, arXiv:2410.06602.

[19] Z. Dong, G. Wang, N. Wang, W.-H. Dong, L. Gu, Y. Xu, J. Cheng, Z. Chen, and Y. Wang, Interstitial oxygen order and its competition with superconductivity in $La_2PrNi_2O_{7+\delta}$, Nat. Mater. **24**, 1927 (2025).

[20] S. L. Dudarev, G. A. Botton, S. Y. Savrasov, C. J. Humphreys, and A. P. Sutton, Electron-energy-loss spectra and the structural stability of nickel oxide: An LSDA + U study, Phys. Rev. B **57**, 1505 (1998).

[21] G. Kresse and J. Furthmüller, Efficient iterative schemes for *ab initio* total-energy calculations using a plane-wave basis set, Phys. Rev. B **54**, 11169 (1996).

[22] J. P. Perdew, K. Burke, and M. Ernzerhof, Generalized gradient approximation made simple, Phys. Rev. Lett. **77**, 3865 (1996).

[23] J. Yang *et al.*, Orbital-dependent electron correlation in double-layer nickelate $La_3Ni_2O_7$, Nat. Commun. **15**, 4373 (2024).

[24] X.-S. Ni, Y. Ji, L. He, T. Xie, D.-X. Yao, M. Wang, and K. Cao, Spin density wave in the bilayered nickelate $La_3Ni_2O_{7-\delta}$ at ambient pressure, npj Quantum Mater. **10**, 17 (2025).

[25] See Supplemental Material at http://link.aps.org/supplemental/10.1103/vhgl-lpwv for computational details and additional results. It also cites [26–29].

[26] E. Abrahams, P. W. Anderson, D. C. Licciardello, and T. V. Ramakrishnan, Scaling theory of localization: Absence of quantum diffusion in two dimensions, Phys. Rev. Lett. **42**, 673 (1979).

[27] A. Weiße, G. Wellein, A. Alvermann, and H. Fehske, The kernel polynomial method, Rev. Mod. Phys. **78**, 275 (2006).

[28] P. A. Lee and T. V. Ramakrishnan, Disordered electronic systems, Rev. Mod. Phys. **57**, 287 (1985).

[29] Z. Luo, X. Hu, M. Wang, W. Wú, and D.-X. Yao, Bilayer two-orbital model of $La_3Ni_2O_7$ under pressure, Phys. Rev. Lett. **131**, 126001 (2023).

[30] M. T. Curnan and J. R. Kitchin, Effects of concentration, crystal structure, magnetism, and electronic structure method on first-principles oxygen vacancy formation energy trends in perovskites, J. Phys. Chem. C **118**, 28776 (2014).

[31] B. Huang, R. Gillen, and J. Robertson, Study of CeO_2 and its native defects by density functional theory with repulsive potential, J. Phys. Chem. C **118**, 24248 (2014).

[32] P. Blaha, K. Schwarz, F. Tran, R. Laskowski, G. K. H. Madsen, and L. D. Marks, WIEN2k: An APW + lo program for calculating the properties of solids, J. Chem. Phys. **152**, 074101 (2020).

[33] A. A. Mostofi, J. R. Yates, G. Pizzi, Y.-S. Lee, I. Souza, D. Vanderbilt, and N. Marzari, An updated version of wannier90: A tool for obtaining maximally-localised Wannier functions, Comput. Phys. Commun. **185**, 2309 (2014).

[34] O. Parcollet, M. Ferrero, T. Ayral, H. Hafermann, I. Krivenko, L. Messio, and P. Seth, TRIQS: A toolbox for research on interacting quantum systems, Comput. Phys. Commun. **196**, 398 (2015).

[35] P. Seth, I. Krivenko, M. Ferrero, and O. Parcollet, TRIQS/CTHYB: A continuous-time quantum Monte Carlo hybridisation expansion solver for quantum impurity problems, Comput. Phys. Commun. **200**, 274 (2016).

[36] M. Aichhorn, L. Pourovskii, P. Seth, V. Vildosola, M. Zingl, O. E. Peil, X. Deng, J. Mravlje, G. J. Kraberger, C. Martins, M. Ferrero, and O. Parcollet, TRIQS/DFTTools: A TRIQS application for *ab initio* calculations of correlated materials, Comput. Phys. Commun. **204**, 200 (2016).

[37] G. J. Kraberger, R. Triebl, M. Zingl, and M. Aichhorn, Maximum entropy formalism for the analytic continuation

of matrix-valued Green's functions, Phys. Rev. B **96**, 155128 (2017).
[38] V. Christiansson, F. Petocchi, and P. Werner, Correlated electronic structure of $La_3Ni_2O_7$ under pressure, Phys. Rev. Lett. **131**, 206501 (2023).
[39] A. Georges, L. d. Medici, and J. Mravlje, Strong correlations from Hund's coupling, Annu. Rev. Condens. Matter Phys. **4**, 137 (2013).
[40] D. A. Shilenko and I. V. Leonov, Correlated electronic structure, orbital-selective behavior, and magnetic correlations in double-layer $La_3Ni_2O_7$ under pressure, Phys. Rev. B **108**, 125105 (2023).
[41] F. Lechermann, J. Gondolf, S. Bötzel, and I. M. Eremin, Electronic correlations and superconducting instability in $La_3Ni_2O_7$ under high pressure, Phys. Rev. B **108**, L201121 (2023).
[42] Y. Cao and Y. F. Yang, Flat bands promoted by Hund's rule coupling in the candidate double-layer high-temperature superconductor $La_3Ni_2O_7$ under high pressure, Phys. Rev. B **109**, L081105 (2024).
[43] Z. Ouyang, J.-M. Wang, J.-X. Wang, R.-Q. He, L. Huang, and Z.-Y. Lu, Hund electronic correlation in $La_3Ni_2O_7$ under high pressure, Phys. Rev. B **109**, 115114 (2024).
[44] Y. Wang, K. Jiang, Z. Wang, F.-C. Zhang, and J. Hu, Electronic and magnetic structures of bilayer $La_3Ni_2O_7$ at ambient pressure, Phys. Rev. B **110**, 205122 (2024).
[45] L. de' Medici, S. R. Hassan, M. Capone, and X. Dai, Orbital-selective Mott transition out of band degeneracy lifting, Phys. Rev. Lett. **102**, 126401 (2009).
[46] E. Jakobi, N. Blümer, and P. G. J. van Dongen, Orbital-selective Mott transitions in a doped two-band Hubbard model with crystal field splitting, Phys. Rev. B **87**, 205135 (2013).
[47] P. Werner, E. Gull, M. Troyer, and A. J. Millis, Spin freezing transition and non-Fermi-liquid self-energy in a three-orbital model, Phys. Rev. Lett. **101**, 166405 (2008).
[48] R. Gao, L. Jin, S. Huyan, D. Ni, H. Wang, X. Xu, S. L. Bud'ko, P. Canfield, W. Xie, and R. J. Cava, Is $La_3Ni_2O_{6.5}$ a bulk superconducting nickelate?, ACS Appl. Mater. Interfaces **16**, 66857 (2024).
[49] V. V. Poltavets, K. A. Lokshin, T. Egami, and M. Greenblatt, The oxygen deficient Ruddlesden-Popper $La_3Ni_2O_{7-\delta}$ ($\delta = 0.65$) phase: Structure and properties, Mater. Res. Bull. **41**, 955 (2006).
[50] W.-S. Wang, Y.-Y. Xiang, Q.-H. Wang, F. Wang, F. Yang, and D.-H. Lee, Functional renormalization group and variational Monte Carlo studies of the electronic instabilities in graphene near 1/4 doping, Phys. Rev. B **85**, 035414 (2012).
[51] Y.-Y. Xiang, F. Wang, D. Wang, Q.-H. Wang, and D.-H. Lee, High-temperature superconductivity at the $FeSe/SrTiO_3$ interface, Phys. Rev. B **86**, 134508 (2012).
[52] W.-S. Wang, Z.-Z. Li, Y.-Y. Xiang, and Q.-H. Wang, Competing electronic orders on kagome lattices at van Hove filling, Phys. Rev. B **87**, 115135 (2013).
[53] W. Metzner, M. Salmhofer, C. Honerkamp, V. Meden, and K. Schönhammer, Functional renormalization group approach to correlated fermion systems, Rev. Mod. Phys. **84**, 299 (2012).
[54] J. Berges, N. Tetradis, and C. Wetterich, Non-perturbative renormalization flow in quantum field theory and statistical physics, Phys. Rep. **363**, 223 (2002).
[55] N. Dupuis, L. Canet, A. Eichhorn, W. Metzner, J. M. Pawlowski, M. Tissier, and N. Wschebor, The nonperturbative functional renormalization group and its applications, Phys. Rep. **910**, 1 (2021).
[56] P. Kopietz, L. Bartosch, and F. Schütz, *Introduction to the Functional Renormalization Group* (Springer, Berlin, 2010).
[57] Q.-G. Yang, D. Wang, and Q.-H. Wang, Possible $s_{\pm}$-wave superconductivity in $La_3Ni_2O_7$, Phys. Rev. B **108**, L140505 (2023).
[58] Q.-G. Yang, K.-Y. Jiang, D. Wang, H.-Y. Lu, and Q.-H. Wang, Effective model and $s_{\pm}$-wave superconductivity in trilayer nickelate $La_4Ni_3O_{10}$, Phys. Rev. B **109**, L220506 (2024).
[59] K.-Y. Jiang, Y.-H. Cao, Q.-G. Yang, H.-Y. Lu, and Q.-H. Wang, Theory of pressure dependence of superconductivity in bilayer nickelate $La_3Ni_2O_7$, Phys. Rev. Lett. **134**, 076001 (2025).
[60] Y.-H. Cao, K.-Y. Jiang, H.-Y. Lu, D. Wang, and Q.-H. Wang, Strain-engineered electronic structure and superconductivity in $La_3Ni_2O_7$ thin films, Sci. China Phys. Mech. Astron. **69**, 247412 (2026).
[61] W. Kohn and J. M. Luttinger, New mechanism for superconductivity, Phys. Rev. Lett. **15**, 524 (1965).
[62] R. Liang, D. A. Bonn, and W. N. Hardy, Growth of YBCO single crystals by the self-flux technique, Philos. Mag. **92**, 2563 (2012).